JPE 18-5-13

https://doi.org/10.6113/JPE.2018.18.5.1434
ISSN(Print): 1598-2092 / ISSN(Online): 2093-4718

Design of Active Disturbance Rejection Control for Inductive Power Transfer Systems

Yanan Wang†, Lei Dong*, Xiaozhong Liao*, Xinglong Ju**, and Furong Xiao***

†,*Department of Automation, Beijing Institute of Technology, Beijing, China
**Beijing Institute of Space Launch Technology, Beijing, China
***Huawei Technologies CO., LTD, Shenzhen, China

Abstract

The control design of inductive power transfer (IPT) systems has attracted a lot of attention in the field of wireless power transmission. Due to the high-order resonant networks and multiple loads in IPT systems, a simplified model of an IPT system is preferred for analysis and control design, and a controller with strong robustness is required. Hence, an active disturbance rejection control (ADRC) for IPT systems is proposed in this paper. To realize the employment of ADRC, firstly a small-signal model of an LC series-compensative IPT system is derived based on generalized state-space averaging (GSSA), then the ADRC is implemented in the designed IPT system. The ADRC not only provides superior robustness to unknown internal and external disturbances, but also requires few knowledge of the IPT system. Due to the convenient realization of ADRC, the designed IPT system retains its simple structure without any additional circuits. Finally, a frequency domain analysis and experimental results have validated the effectiveness of the employed ADRC, especially its robustness in the presence of frequency drifts and other common disturbances.

Key words: Active disturbance rejection control, Frequency drift, Generalized state-space averaging, Inductive power transfer, Small-signal model

I. INTRODUCTION

Inductive power transfer (IPT) systems (see Fig. 1) are widely employed to deliver power to loads over a relatively large air gap via magnetic coupling. This technology has been applied in home appliances [1], [2], implantable devices [3], [4], and electrical vehicles [5]-[7]. The control design of IPT systems has always been a key issue in previous research, most of which focused on the power transfer capability and the output voltage controllability at the Rx side [8]-[11]. Generally, both Tx sidee and Rx side of a IPT system require a controller [12], [13], which results in a complex control strategy for the IPT system. To facilitate the information synchronization between Tx and Rx sides, some researchers have tried to implement communication by frequency-shift keying (FSK) and magnitude-shift keying (ASK) [14], an auxiliary coil in the pick-up side [15], or the use of transfer coupling coils [16]. However, these design methods have complicated system structures and consume significant resources. To deal with these issues, some intelligent techniques, such as an improved ant colony algorithm, adaptive sliding-mode control, particle swarm optimization, and PID controller tuning by neural networks, have been proposed for IPT systems [17]-[20]. However, these intelligent methods just shift the complication of the control design from hardware to software. In addition, they always suffer from tedious codes.

Some previous studies have focused on research of the Tx side, such as the influence analysis of Tx coils [21], robust Tx design [22], and constant primary current operation [23]. The stability and robustness of the Tx side deserves more research, especially for dynamic EV charging systems [24], [25], which require independence of the Rx side. Therefore, a method to enhance the robustness of IPT systems is a key point of the involved control design.

Manuscript received Nov.14, 2017; accepted Apr. 2, 2018
Recommended for publication by Associate Editor Hao Ma.
†Corresponding Author: correspondent_dong@163.com
Tel: +86-1068912460, Beijing Institute of Technology
*Department of Automation, Beijing Institute of Technology, China
**Beijing Institute of Space Launch Technology, China
***Huawei Technologies CO., LTD, China

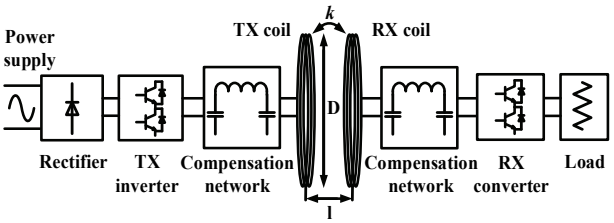

Fig. 1. Typical IPT system.

In light of the above-mentioned issues, an active disturbance rejection control (ADRC) method is presented for IPT systems in this paper. Considering high-order resonant networks, it is always difficult to obtain accurate non-linear models of IPT systems. Consequently, dynamic models for IPT systems have been developed based on state space [26], [27], and a simplified current model is drawn for the employment of ADRC. In the literature, there are two common types of current modeling methods, discrete time-mapping modeling [28], and generalized state-space averaging (GSSA) modeling [29]. Because GSSA can transform a nonlinear model in the time domain into a linear state space model in the frequency domain, this method is particularly suitable for the control design of full resonant converters [30], [31].

Hence, a small-signal model of a typical IPT system is derived on the basis of GSSA in this paper. Then the detailed design process of the ADRC and a robustness analysis of the close-loop system are presented. Converting all of the Rx side circuits as a reflected voltage to the Tx side, the ADRC is only employed in the Tx side controller of an IPT system, which simplifies the design of controller. Moreover, due to the convenient realization of the ADRC, the designed IPT system retains its simple structure without any additional circuits. Finally, the effectiveness of the proposed ADRC has been demonstrated through experimental results. Since the ADRC only requires a little knowledge of the controlled IPT system, it can be applied to any IPT systems with the typical structure shown in Fig. 1, such as the dynamic EV charging systems.

II. PRELIMINARY

A. Generalized State-Space Averaging

To realize the dynamic control of ADRC, a small-signal linear model should be derived to approximate the nonlinear part of an IPT system. Both generalized state-space averaging (GSSA) [32] and state-space averaging (SSA) have been widely applied to derive small-signal models of pulse-width modulated power converters. Since SSA is inapplicable to calculating the AC state variables of the illustrated IPT system, GSSA is adopted to derive the small-signal model in this paper. It is worth mentioning that GSSA is based on the fact that a given waveform $x(t)$ in the interval $(t-T, t]$ can be approximated with any desired accuracy by using a complex Fourier series expression as:

$$x(t \to T+\tau) = \sum_k \langle x \rangle_k(t) \mathrm{e}^{\mathrm{j}k\omega(t-T+\tau)} \tag{1}$$

where the sum is over all of the integers k, $\omega = 2\pi/\mathrm{T}, \tau \in (0, T]$, T corresponds to the period of the fundamental harmonic, and $\langle x \rangle_k$ is the k_{th} complex Fourier coefficient, which is determined by:

$$\langle x \rangle_k(t) = \frac{1}{T}\int_0^T x(t-T+\tau)\mathrm{e}^{-\mathrm{j}k\omega(t-T+\tau)}\mathrm{d}\tau \tag{2}$$

The objective of GSSA is to determine an appropriate state-space model in which the coefficients in Equ. (2) are state variables. Assume that the time-domain nonlinear differential model of a typical converter system is shown as:

$$\frac{d}{dt}x(t) = f\big(x(t), u(t)\big) \tag{3}$$

where $x(t) = [x_1, x_2, \cdots, x_i]^T$ are the state variables and $u(t) = [u_1, u_2, \cdots, u_i]$ is the input. Based on the time derivative characteristics, Equ. (3) can be derived as:

$$\frac{d}{dt}\langle x \rangle_k(t) = \langle f\big(x(t), u(t)\big)\rangle_k(t) - jk\omega\langle x \rangle_k(t) \tag{4}$$

Linearizing $\langle f\big(x(t), u(t)\big)\rangle_k(t)$ by the convolution characteristics, Equ. (4) can be derived as a state-space model:

$$\frac{d}{dt}x(t) = \boldsymbol{A}x(t) + \boldsymbol{B}u(t) \tag{5}$$

where $x(t)$ can be represented as the real part and imaginary part separately. Then state matrix $\boldsymbol{A}$ and input matrix $\boldsymbol{B}$ can be obtained by solving Equ. (5). Hence, given the nonlinear differential model of the resonant converter in the time domain, the GSSA model can be derived as a state-space model with the state variables represented by complex Fourier components. It is important to note that the inputs and outputs of the GSSA model are the RMS values of actual signals averaged over a period defined by kT. Unlike SSA, GSSA is not subject to the assumption that input variables vary slowly [33]. Consequently, GSSA can be applied to the modeling and analysis of a lot more kinds of IPT systems. Especially, the GSSA method is suitable for low-order (below 5$^{\text{th}}$) resonant converters [29].

B. Active Disturbance Rejection Control

Active disturbance rejection control (ADRC) was first proposed by Professor Han to combine the advantages of PID control and modern control theory [34]. By estimating the total system disturbances, ADRC compensates the system with linear or nonlinear feedback in real-time. The framework of ADRC is shown in Fig. 2, where X is the reference input, z_1, z_2 and z_3 are the estimated state variables, b_0 is the compensation factor, and y is the output. ADRC generally consists of a transient process, an extended state observer (ESO), a disturbance compensation unit and a control law.

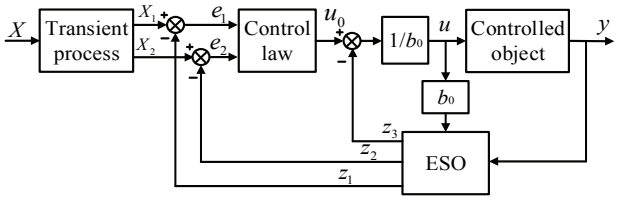

Fig. 2. Framework of ADRC.

The constraints and the order of the controlled plant should be considered to design a suitable transient process [34], which is relatively complex for IPT systems. Hence, the transient process is not used in the proposed ADRC for IPT systems in this paper.

1) Extended State Observer

Generally, an extended state observer (ESO) is adopted to estimate the state variables of the considered system. Denote $f(x_1, x_2, t)$ as an unknown disturbance of a second-order system that needs to be estimated. Then the third-order ESO can be obtained as:

$$\begin{cases} e = z_1 - y \\ \dot{z}_1 = z_2 - \beta_{01} g_1(e) \\ \dot{z}_2 = z_3 - \beta_{02} g_2(e) + b_0 u \\ \dot{z}_3 = -\beta_{03} g_3(e) \end{cases} \tag{6}$$

where z_1, z_2 and z_3 are the estimated state variables of x_1, x_2 and $f(x_1, x_2, t)$, respectively. With suitable parameters β_{01}, β_{02}, β_{03} and functions $g_1(e)$, $g_2(e)$, $g_3(e)$, the steady-state error e can be negligible, and the unknown disturbance $f(x_1, x_2, t)$ can be estimated by the ESO.

2) Disturbance Compensation and Control Law

As mentioned above, to eliminate the influence of the disturbance $f(x_1, x_2, t)$, the extended state z_3 is adopted as a negative feedback to the control system as shown in Fig. 2. Thus, the disturbance can be compensated as:

$$u = \frac{u_0 - z_3}{b_0} \tag{7}$$

Assuming $z_3 \approx f(x_1, x_2, t)$, the second-order system becomes an integrators series system $\ddot{x} \approx b_0 u_0$. After that, a PID controller or a nonlinear control law can be adopted as the control law to achieve acceptable performance. In summary, ADRC does not depend on an accurate system model, and it considers all unknown components as disturbances to be estimated and compensated. Hence, ADRC is particularly suitable for the illustrated IPT system, whose accurate mathematic model is difficult to derive due to the nonlinear part of the system.

III. Active Disturbance Rejection Control Based Inductive Power Transfer System

The LC series resonant tank, which is susceptible to external disturbances, such as load variations and frequency drifts, is considered in the designed IPT system. By applying ADRC to an IPT system with an LC series resonant tank in the transmitting (Tx) circuit, this section aims to derive the structure of the IPT system with integrated ADRC and to verify the robustness of the close-loop system. A small-signal model of the IPT system is derived from a GSSA model. Then the design and an analysis of the developed ADRC controller are presented.

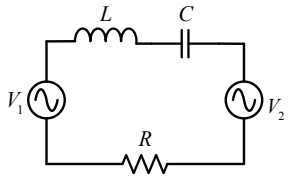

Fig. 3. Simplified model of an IPT system with an LC series Tx resonant tank. V_1 is the input AC voltage source, L and C are the resonant inductor and capacitor, respectively, and R is the equivalent resistance of the Tx circuit. The effect of the receiver is abstracted as a reflected voltage V_2.

A. Small-Signal Model of an IPT System

It should be mentioned that, in IPT systems, the receiving (Rx) circuit structure including a secondary controller, the coupling coefficient or load may change in different situations. Hence, a conventional small-signal model considering only a certain Rx topology is not suitable for IPT systems. In fact, the influence of the Rx circuit on the transmitter side is equivalent to a reflected voltage in the Tx coil [26], [31], which can be considered as a disturbance when modeling the Tx circuit. In this way, the modeling of the Tx circuit is independent of the receiving circuit topology. A simplified model of the IPT system can be obtained as shown in Fig. 3.

Despite the Rx circuit structure, an AC inductive voltage V_2 generated in the Tx coil is used to represent the influence of the Rx circuit on the Tx side. From Fig. 3, differential equations of the LC series-compensative IPT system can be achieved as:

$$\begin{cases} V_1 sig[\sin(\omega t)] = R i_L(t) + L\frac{di_L(t)}{dt} + V_c(t) + V_2 \sin(\omega t + \theta) \\ C\frac{dV_c(t)}{dt} = i_L(t) \end{cases} \tag{8}$$

where the AC input voltage V_1, generated by switch actions of the inverter, is actually a square signal, which is presented as a combination of the sign function $sig(x)$ and the sine function $\sin(x)$. Assuming that the Tx and Rx circuits are working at the resonant frequency, all of the voltages and currents, including the inductive voltage V_2, can be represented as sinusoidal values. In addition, θ is the phase difference between V_1 and V_2. Replace the variables of Equ. (8) with their complex Fourier series representations as:

$$i_L(t) = \sum_{k=-\infty}^{+\infty} \langle i_L \rangle_k(t) e^{jk\omega_0 t},\ v_c(t) = \sum_{k=-\infty}^{+\infty} \langle v_c \rangle_k(t) e^{jk\omega_0 t}$$
$$sig[\sin(\omega t)] \approx -\frac{2j}{\pi},\ \sin(\omega t + \theta) \approx \frac{V_2}{2}(-j\cos\theta + \sin\theta) \tag{9}$$

where ω_0 is the fundamental frequency. Provided that the higher order harmonics are negligible, the IPT system can be approximately modeled based on fundamental complex Fourier components, which correspond to $k=-1,+1$. Considering the conjugate symmetry of the Fourier series, $\langle i_L\rangle_1=\langle i_L\rangle_{-1}$, and $\langle v_c\rangle_1(t)=\langle v_c\rangle_{-1}(t)$, Equ. (8) can be rewritten with the fundamental positive component ($k=1$) as:

$$\begin{cases}\frac{d}{dt}\langle i_L\rangle_1(t)=-\mathrm{j}\omega\langle i_L\rangle_1(t)-\frac{V_2}{2L}[\sin\theta-\mathrm{j}\cos\theta]\\ \qquad -\left[\frac{2V_1\mathrm{j}}{\pi L}+\frac{1}{L}\langle i_L\rangle_1(t)R+\frac{1}{L}\langle v_c\rangle_1(t)\right]\\ \frac{d}{dt}\langle v_c\rangle_1(t)=-\mathrm{j}\omega\langle v_c\rangle_1(t)+\frac{1}{C}\langle i_L\rangle_1(t)\end{cases} \tag{10}$$

Denote the real and imaginary parts of $\langle i_L\rangle_1(t)$ and $\langle v_c\rangle_1(t)$ as $\langle i_L\rangle_{1\mathrm{re}}(t)$, $\langle i_L\rangle_{1\mathrm{im}}(t)$, $\langle v_c\rangle_{1\mathrm{re}}(t)$ and $\langle v_c\rangle_{1\mathrm{im}}(t)$, respectively. Then the general averaged state variables are defined as:

$$\begin{aligned}X&=[x_1,x_2,x_3,x_4]^{\mathrm{T}}\\&=[\langle i_L\rangle_{1\mathrm{re}}(t),\langle i_L\rangle_{1\mathrm{im}}(t),\langle v_c\rangle_{1\mathrm{re}}(t),\langle v_c\rangle_{1\mathrm{im}}(t)]^{\mathrm{T}}\end{aligned} \tag{11}$$

To clearly illustrate the influence of the Rx circuit, $\sin(\theta)V_2$ and $cos(\theta)V_2$ are denoted as $V_{2\mathrm{re}}$ and $V_{2\mathrm{im}}$, respectively. By substituting Equ. (11) into Equ. (10), the GSSA model of the LC series-compensative IPT system can be derived as:

$$\begin{bmatrix}\dot{x}_1\\ \dot{x}_2\\ \dot{x}_3\\ \dot{x}_4\end{bmatrix}=\begin{bmatrix}-\frac{R}{L} & \omega & -\frac{1}{L} & 0\\ -\omega & -\frac{R}{L} & 0 & -\frac{1}{L}\\ \frac{1}{C} & 0 & 0 & \omega\\ 0 & \frac{1}{C} & -\omega & 0\end{bmatrix}\begin{bmatrix}x_1\\ x_2\\ x_3\\ x_4\end{bmatrix}+\begin{bmatrix}0 & -\frac{1}{2L} & 0\\ -\frac{2}{\pi L} & 0 & \frac{1}{2L}\\ 0 & 0 & 0\\ 0 & 0 & 0\end{bmatrix}\begin{bmatrix}V_1\\ V_{2\mathrm{re}}\\ V_{2\mathrm{im}}\end{bmatrix} \tag{12}$$

Note that the resonant current is approximated as the sum of the fundamental complex Fourier components, which correspond to $2\langle i_L\rangle_1(t)cos\omega_0 t$. Thus, the magnitude and RMS of the resonant current are given by:

$$i_{track}=|i_L(t)|=2\sqrt{x_1^2+x_2^2} \tag{13}$$

$$I_{track}=\sqrt{2}\sqrt{x_1^2+x_2^2} \tag{14}$$

To illustrate the response of the resonant current to a disturbance in V_2, a small-signal model of the theoretical GSSA model is derived by replacing each of the state variables and the input to the GSSA model with their steady-state and small disturbance terms as:

$$x_n=x_{n,\mathrm{ss}}+\tilde{x}_n,\ (n=1,2,3,4) \tag{15}$$

$$V_m=V_{m,\mathrm{ss}}+\tilde{V}_m,(m=1,2) \tag{16}$$

Substituting Equ. (15) and Equ. (16) into Equ. (12), the derived small-signal model is:

$$\begin{bmatrix}\dot{\tilde{x}}_1\\ \dot{\tilde{x}}_2\\ \dot{\tilde{x}}_3\\ \dot{\tilde{x}}_4\end{bmatrix}=\begin{bmatrix}-\frac{R}{L} & \omega & -\frac{1}{L} & 0\\ -\omega & -\frac{R}{L} & 0 & -\frac{1}{L}\\ \frac{1}{C} & 0 & 0 & \omega\\ 0 & \frac{1}{C} & -\omega & 0\end{bmatrix}\begin{bmatrix}\tilde{x}_1\\ \tilde{x}_2\\ \tilde{x}_3\\ \tilde{x}_4\end{bmatrix}+\begin{bmatrix}0 & -\frac{1}{2L} & 0\\ -\frac{2}{\pi L} & 0 & \frac{1}{2L}\\ 0 & 0 & 0\\ 0 & 0 & 0\end{bmatrix}\begin{bmatrix}\tilde{V}_1\\ \tilde{V}_{2re}\\ \tilde{V}_{2im}\end{bmatrix} \tag{17}$$

The magnitude and RMS of the resonant current are also represented in small-signal forms as:

$$\tilde{\imath}_{\mathrm{track}}=\frac{2x_{1,\mathrm{ss}}}{\sqrt{x_{1,\mathrm{ss}}^2+x_{1,\mathrm{ss}}^2}}\tilde{x}_1+\frac{2x_{2,\mathrm{ss}}}{\sqrt{x_{1,\mathrm{ss}}^2+x_{2,\mathrm{ss}}^2}}\tilde{x}_2 \tag{18}$$

$$\tilde{I}_{\mathrm{track}}=\frac{\sqrt{2}x_{1,\mathrm{ss}}}{\sqrt{x_{1,\mathrm{ss}}^2+x_{2,\mathrm{ss}}^2}}\tilde{x}_1+\frac{\sqrt{2}x_{2,\mathrm{ss}}}{\sqrt{x_{1,\mathrm{ss}}^2+x_{2,\mathrm{ss}}^2}}\tilde{x}_2 \tag{19}$$

The derived small-signal model of the LC series-compensative IPT system describes how the resonant tracking current responds to a disturbance in V_2, and these RMS values are all averaged over a resonant period.

B. IPT System with ADRC

To apply ADRC to an LC series-compensative IPT system, the control object of the small-signal model should be RMS values and expressed in the form of Equ. (11). For IPT systems, the resonant current represents the injected power to the Tx tank, and its robustness confirms the stability of the whole system, both of which were the focus of previous studies [12], [15], [31]. Moreover, control of the RMS value of the resonant current can ensure a stable power output from the Tx tank to the Rx side, and it would not be affected by different Rx circuits or loads. Therefore, the RMS value of the resonant current was chosen as the control object of the ADRC in this paper. Assume that $y=\tilde{I}_{\mathrm{track}}$, and calculate the derivation of Equ. (19) as:

$$\dot{y}=\frac{\sqrt{2}x_{1,\mathrm{ss}}}{\sqrt{x_{1,\mathrm{ss}}^2+x_{2,\mathrm{ss}}^2}}\dot{\tilde{x}}_1+\frac{\sqrt{2}x_{2,\mathrm{ss}}}{\sqrt{x_{1,\mathrm{ss}}^2+x_{2,\mathrm{ss}}^2}}\dot{\tilde{x}}_2 \tag{20}$$

Substituting Equ. (17) into Equ. (20) yields:

$$\begin{aligned}\dot{y}=&\frac{\sqrt{2}x_{1,\mathrm{ss}}}{\sqrt{x_{1,\mathrm{ss}}^2+x_{2,\mathrm{ss}}^2}}[\omega\tilde{x}_2-\frac{1}{L}(\tilde{x}_1R+\tilde{x}_3)-\frac{\tilde{V}_{2\mathrm{re}}}{2L}]+\\&\frac{\sqrt{2}x_{2,\mathrm{ss}}}{\sqrt{x_{1,\mathrm{ss}}^2+x_{2,\mathrm{ss}}^2}}[-\omega\tilde{x}_1-\frac{1}{L}(\frac{2\tilde{V}_1}{\pi}+\tilde{x}_2R+\tilde{x}_4)+\frac{\tilde{V}_{2\mathrm{im}}}{2L}]\end{aligned} \tag{21}$$

Based on ADRC, the unknown parameters, state variables, and disturbances are regarded as equivalent disturbances. In Equ. (21), the known input voltage V_1 acts as the control input, which aims to eliminate perturbations of the RMS resonant current caused by disturbances, that is y=0. Then Equ. (21) is rewritten as:

$$\dot{y}=f(\tilde{x}_1,\tilde{x}_2,\tilde{x}_3,\tilde{x}_4,V_{2\mathrm{re}},V_{2\mathrm{im}},x_{1,\mathrm{ss}},x_{2,\mathrm{ss}})-\frac{2\sqrt{2}x_{2,\mathrm{ss}}}{\pi L\sqrt{x_{1,\mathrm{ss}}^2+x_{2,\mathrm{ss}}^2}}V_1 \tag{22}$$

1) Extended State Observer

In this subsection, a second-order ESO is established for

the controlled object shown in Equ. (22) as:

$$\begin{cases} e = z_1 - y \\ \dot{z}_1 = z_2 - \beta_1 e + b_0 V_1 \\ \dot{z}_2 = -\beta_2 e \end{cases} \tag{23}$$

where β_1 and β_2 are gain factors that are adjustable, $b_0 = -2\sqrt{2}x_{2,\mathrm{ss}}/(\pi L\sqrt{x_{1,\mathrm{ss}}^2 + x_{2,\mathrm{ss}}^2})$which is the compensation factor. Transferring Equ. (23) into the state space representation yields:

$$\begin{bmatrix} \dot{z}_1 \\ \dot{z}_2 \end{bmatrix} = \begin{bmatrix} -\beta_1 & 1 \\ -\beta_2 & 0 \end{bmatrix} \begin{bmatrix} z_1 \\ z_2 \end{bmatrix} + \begin{bmatrix} \beta_1 & b_0 \\ \beta_2 & 0 \end{bmatrix} \begin{bmatrix} y \\ V_1 \end{bmatrix} \tag{24}$$

Thus, the transfer functions of Equ. (24) can be achieved as:

$$z_1(s) = \frac{s\beta_1+\beta_2}{s^2+s\beta_1+\beta_2} Y(\mathrm{s}) + \frac{b_0 s}{s^2+s\beta_1+\beta_2} V_1(s) \tag{25}$$

$$z_2(s) = \frac{s\beta_2}{s^2+s\beta_1+\beta_2} Y(\mathrm{s}) - \frac{b_0\beta_2}{s^2+s\beta_1+\beta_2} V_1(s) \tag{26}$$

According to the parameter tuning guidance of ADRC proposed by Prof. Gao Zhiqiang [35], β_1 and β_2 can be expressed as functions of the bandwidth of the ESO ω_b, i.e. $\beta_1 = 2\omega_\mathrm{b}$ and $\beta_2 = \omega_\mathrm{b}^2$. Then the characteristic equations of Equ. (25) and Equ. (26) are in the form of $(s+\omega_\mathrm{b})^2$ to ensure the stability of the ESO.

2) Disturbance Compensation and Control Law

According to Part *B* of section II, the estimated value of an unknown disturbance $f(\tilde{x}_1, \tilde{x}_2, \tilde{x}_3, \tilde{x}_4, V_{2\mathrm{re}}, V_{2\mathrm{im}}, x_{1,\mathrm{ss}}, x_{2,\mathrm{ss}})$, that is $z_2(s)$, is fed back into the ADRC based system for compensating the unknown disturbance as:

$$u(s) = \frac{u_0(s) - z_2(s)}{b_0} \tag{27}$$

It is worth noting that there is only one feedback signal $z_1(s)$ to the controller part, and that the controlled IPT system is transferred into a first-order pure integral system with the ESO and disturbance compensation unit. Hence, the P controller is sufficient to apply as a control law. Based on Equs. (25)-(27), the framework of the LC series- compensative IPT system with ADRC can be derived as shown in Fig. 4. In this figure, $Q_1(s) = \frac{b_0 s}{s^2+s\beta_1+\beta_2}$, $P_1(s) = \frac{s\beta_1+\beta_2}{s^2+s\beta_1+\beta_2}$, $Q_2(s) = \frac{b_0\beta_2}{s^2+s\beta_1+\beta_2}$, $P_2(s) = \frac{s\beta_2}{s^2+s\beta_1+\beta_2}$, and K is the proportional-gain of the P controller. $G_i(\mathrm{s})$ is the transfer function from the voltage $V_i(s)$ to the RMS value of the resonant current $Y(s)$, and is given by:

$$G_i(\mathrm{s}) = A\frac{\tilde{x}_1}{\tilde{V}_i(s)} + B\frac{\tilde{x}_2}{\tilde{V}_i(s)},\ (i = 1,2\mathrm{re}, 2\mathrm{im}) \tag{28}$$

where $A = \frac{\sqrt{2}x_{1,\mathrm{ss}}}{\sqrt{x_{1,\mathrm{ss}}^2+x_{2,\mathrm{ss}}^2}}$, $B = \frac{\sqrt{2}x_{2,\mathrm{ss}}}{\sqrt{x_{1,\mathrm{ss}}^2+x_{2,\mathrm{ss}}^2}}$, and the transfer functions $\frac{\tilde{x}_1}{\tilde{V}_i(s)}$ and $\frac{\tilde{x}_2}{\tilde{V}_i(s)}$ can be derived from Equ. (17) by $G(s) = C(sI - A)^{-1}B + D$. From Fig. 4, the transfer function from $u_0(\mathrm{s})$ to $Y(s)$ is:

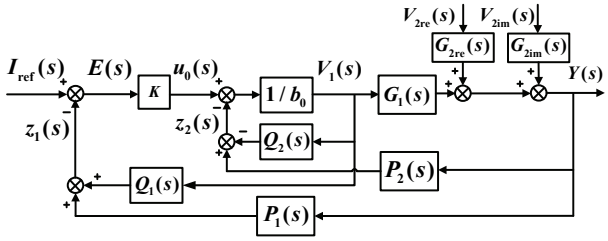

Fig. 4. Framework of an LC series-compensative IPT System with ADRC.

$$G_c(s) = \frac{Y(s)}{u_0(s)} = \frac{G_1(s)}{b_0 - Q_2(s) + P_2(s)G_1(s)} \tag{29}$$

The transfer function from $E(s)$ to $z_1(s)$, which is the feedback gain, is:

$$G_{C1}(s) = \frac{z_1(s)}{E(s)} = K\frac{Q_1(s) + P_1(s)G_1(s)}{b_0 - Q_2(s) + G_1(s)P_2(s)} \tag{30}$$

Thus, the close-loop transfer function from $I_\mathrm{ref}(s)$ to $Y(s)$ is:

$$G_{cl}(s) = \frac{\mathrm{Y(s)}}{I_{ref}(s)} = \frac{K \cdot G_C(s)}{1 + G_{C1}(s)} \tag{31}$$

Similarly, the transfer function from the disturbance $D_i(s)$ of $V_{2\mathrm{re}}(s)$ or $V_{2\mathrm{im}}(s)$ to $Y(s)$ is:

$$G_{Di}(s) = \frac{\mathrm{Y(s)}}{D_i(s)} = \frac{G_i(\mathrm{s})[b_0 - Q_2(\mathrm{s}) + KQ_1(\mathrm{s})]}{[b_0 - Q_2(\mathrm{s}) + KQ_1(\mathrm{s})] + G_1(\mathrm{s})[KP_1(\mathrm{s}) + P_2(\mathrm{s})]},\ (i = 2\mathrm{re}, 2\mathrm{im}) \tag{32}$$

C. Simulation Verification

To analyze the robustness of the proposed IPT system with ADRC, magnitude-frequency curves of the close-loop system are drawn with different inductive voltages or frequency drifts. Considering the following four different working situations:

(a) Situation 1: assume that the parameters of the Tx resonant tank are $L = 100\mu\mathrm{H}$, $C = 0.1\mu\mathrm{F}$ and $R = 1\Omega$, the magnitude of the input voltage V_1 is 100V, the magnitude of inductive voltage V_2 is 50V, and the phase difference between V_1 and V_2 is $\theta = -20°$. The corresponding steady-states are $x_{1,\mathrm{ss}} = 22.1$ and $x_{2,\mathrm{ss}} = -30.32$ as calculated by Equ. (12).

(b) Situation 2: assume that the inductive voltage is influenced by load changes, which turns to be $V_2 = 30V$, $\theta = -10°$, and the other parameters stay the same as situation 1. The corresponding steady-states are $x_{1,\mathrm{ss}} = 20.4$ and $x_{2,\mathrm{ss}} = -39.8$.

(c) Situation 3: assume that the parameters of the Tx resonant tank are changed to $L = 90.91\mu\mathrm{H}$, $C = 0.09091\mu\mathrm{F}$ and $R = 1\Omega$, which causes a 10% frequency drift from the 50kHz working frequency. The inductive voltage remains $V_2 = 30V$, $\theta = -10°$. The corresponding steady-states are

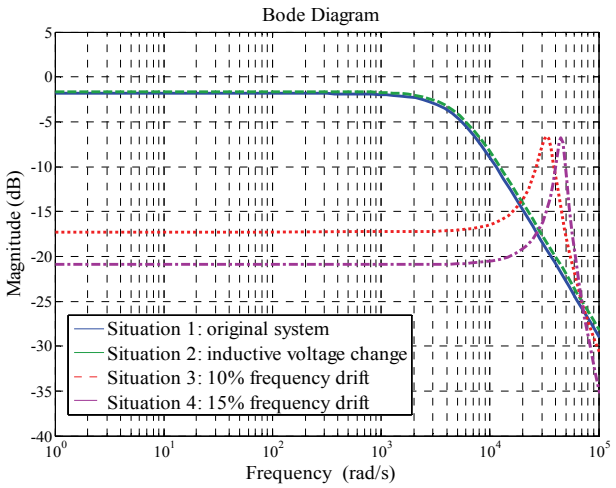

Fig. 5. Magnitude-frequency curve of $G_1(s)$.

$x_{1,ss} = 5.78$ and $x_{2,ss} = -1.56$.

(d) Situation 4: assume that the parameters of the Tx resonant tank is changed to $L = 117.65\mu H$, $C = 0.11765\mu F$, and $R = 1\Omega$, which causes a 15% frequency drift from the 50kHz working frequency. The inductive voltage is $V_2 = 50V$, $\theta = -10°$. The corresponding steady-states are $x_{1,ss} = -3.87$ and $x_{2,ss} = -0.83$.

Taking all of the parameters of the four situations into Equ. (28), Equs. (30)-(32), the transfer function $G_1(s)$, $G_{C1}(s)$, $G_{cl}(s)$ and $G_D(s)$ can be calculated. Then the magnitude-frequency curves are drawn. It should be noted that the working frequency remains 50kHz in the four situations, the bandwidth of the ESO is $\omega_b = 400\pi$ kHz, and the proportional-gain is $K = 2000$. Fig. 5 shows a magnitude-frequency curve of $G_1(s)$, which is the transfer function of the IPT system without ADRC. From Fig. 5, when the IPT system works on the resonant frequency, the changes of the inductive voltage have little influence on the open-loop gain of the IPT system.

However, frequency drifts result in a large decrease of the open-loop gain. The larger the frequency drift, the larger the decrease of the open-loop gain. Hence, a method to retain the robustness of an IPT system with frequency drift is an important issue for the IPT systems. Fig. 6 and Fig. 7 show the magnitude-frequency curves of $G_{C1}(s)$ and $G_{cl}(s)$, which are the feedback gain and close-loop transfer function of the IPT system with ADRC, respectively. From Fig. 6 and Fig. 7, it is obvious that both the feedback gain and the close-loop gain remain approximately the same, which verifies that ADRC can help the IPT system maintain strong robustness against the frequency drift caused by resonant parameters.

Fig. 8 and Fig. 9 are magnitude-frequency curves of $G_{D2re}(s)$ and $G_{D2im}(s)$, and they reflect the influence of $V_{2re}(s)$ and $V_{2im}(s)$ on the resonant current, respectively. From Fig. 8 and Fig. 9, it can be concluded that ADRC can effectively stabilize the IPT system against perturbations of

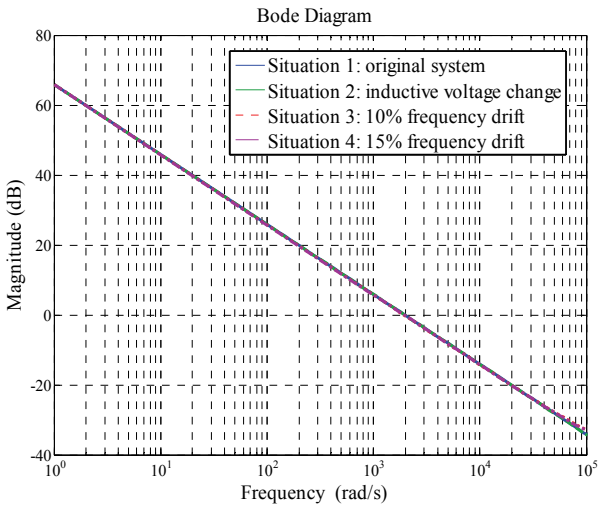

Fig. 6. Magnitude-frequency curve of the feedback gain $G_{C1}(s)$.

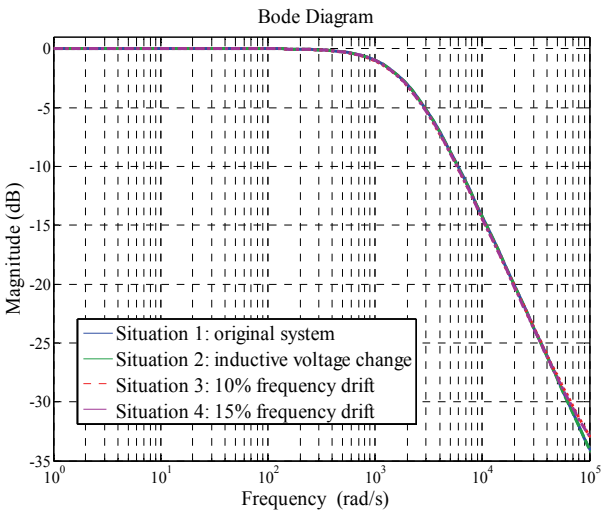

Fig. 7. Magnitude-frequency curve of the close-loop transfer function $G_{cl}(s)$.

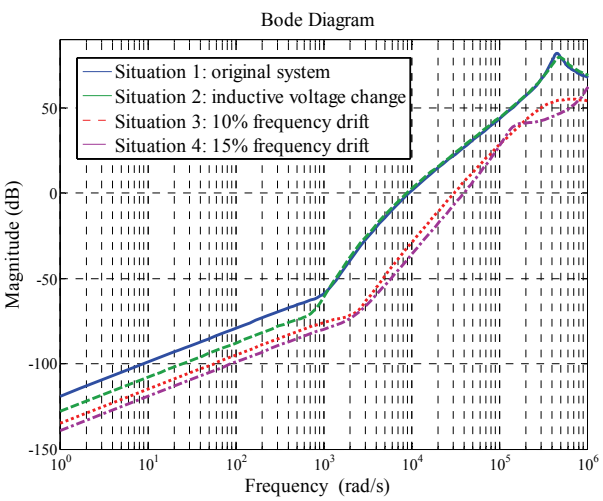

Fig. 8. Magnitude-frequency curve of $G_{D2re}(s)$.

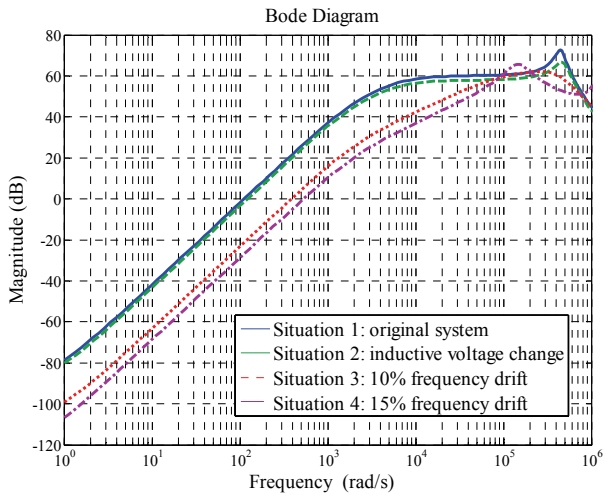

Fig. 9. Magnitude-frequency curve of $G_{D2\mathrm{im}}(s)$.

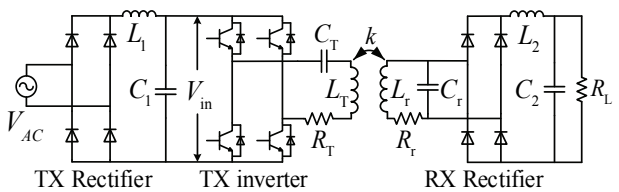

Fig. 10. Integral LC series-compensative IPT system with Rx circuits and a load.

the inductive voltage. Hence, it suggests that IPT systems with ADRC can maintain strong robustness against the inductive voltage disturbances caused by different loads in practical IPT systems. However, it should be noted that the control ability of ADRC is relatively weakened when the frequency drift occurs.

IV. Experimental Results

To validate the performance of the proposed LC series-compensative IPT System with ADRC, an Rx resonant circuit and a resistive load were employed to construct an integral IPT system as shown in Fig. 10. In addition, the constructed prototype is shown in Fig. 11. Tx and Rx coils with a 200mm inner diameter were fabricated with 1.92mm diameter Litz wires. Since the focus of this paper is the robust control of Tx resonant current, the air gap between the two coils was set as 90mm in all of the experiments.

IGBTs FGA25N120 and rectifier (diodes) KBPC2510 were employed. The other key parameters of the prototype are listed in Table I.

In practical IPT systems, inductive voltage disturbances from loads, changes of the Rx tank capacitors, and frequency drift can all be regarded as disturbances in the ADRC control. Hence, the proposed ADRC based IPT system is tested under step responses, load disturbances, and Rx resonant capacitor disturbances. The controlled object, the RMS value of the Tx

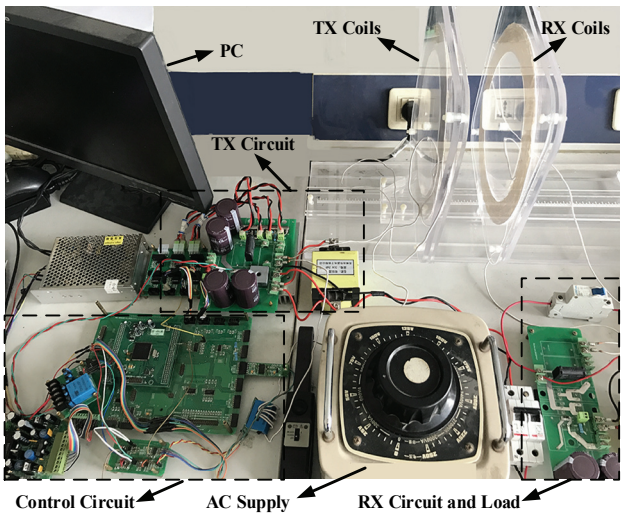

Fig. 11. Experimental setup.

TABLE I
Key Parameters of the Experimental Setup

Parameters	Value
AC supply voltage V_{AC}	90V
Reference of Tx resonant current I_{ref}	4A
Inductance L_1, L_2	2mH
Capacitors C_1, C_2	940μF
Tx resonant inductance L_{T}	0.1mH
Tx resonant capacitor C_{T}	0.12μF(46kHz) 0.1μF(50kHz) 0.08μF(56kHz)
Tx resonant resistor R_{T}	0.1Ω
Rx resonant inductance L_{r}	0.1mH
Rx resonant capacitor C_{r}	0.1μF
Rx resonant resistor R_{r}	0.1Ω
Coupling coefficient k	0.19
Load resistor R_{L}	152Ω

resonant current, is calculated through a RMS computing filter for AC waveforms and sampled by a DSP F28335. By the ADRC control of the DSP, the Tx inverter switches are regulated to make the Tx resonant current track the reference. For comparison, the same experiments were also conducted in an IPT system with PI control. After being well tuned by the method in [35], the parameters of ADRC are $\beta_1 = 100$, $\beta_2 = 3200$, $b_0 = 20$ and $K = 4$ (the P controller of the control law). The parameters of the PI controller are optimized based on the index integral time absolute error (ITAE). That is, the proportional gain $K_{\mathrm{p}} = 3$, and the integral gain $K_{\mathrm{i}} = 0.24$. Both the ADRC and PI controllers are employed in the following experiments.

A. Step Response

Figs. 12-14 depict the measured resonant waveforms and step responses of IPT systems with ADRC and with PI control. In this case, the working frequency of the Tx inverter

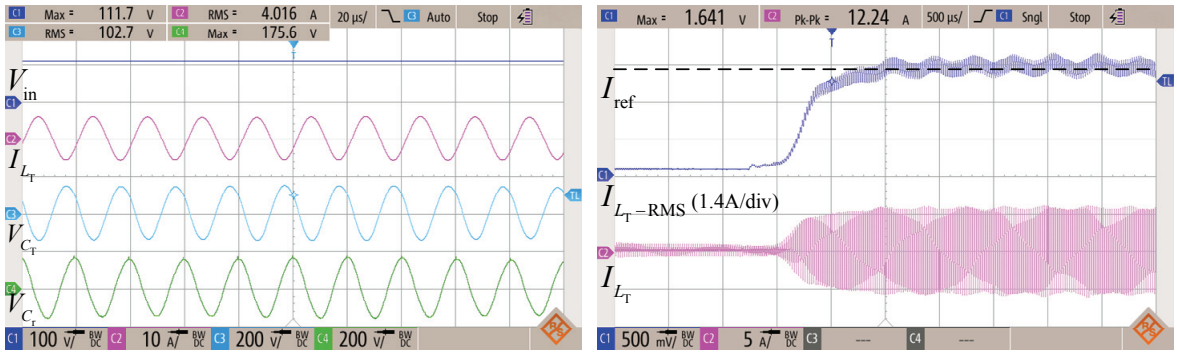

(a)

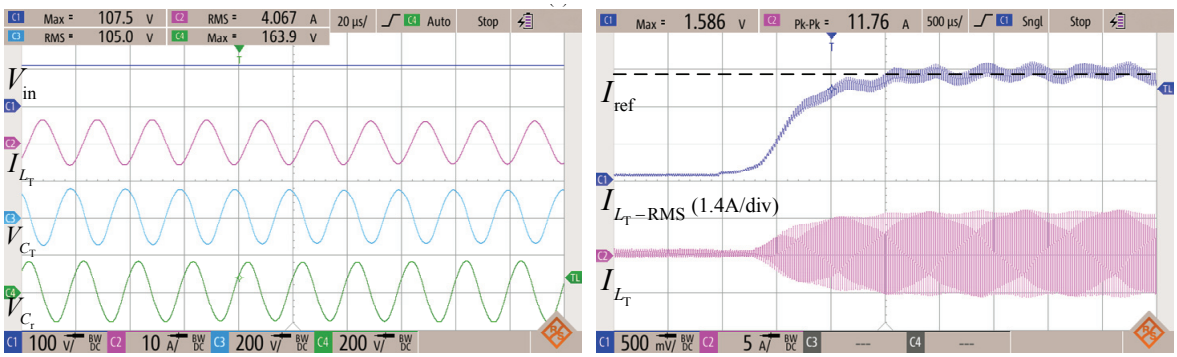

(b)

Fig. 12. Measured DC input voltage, resonant waveforms, and the step response of an IPT system with $f_T = 46$kHz, while f_0 remains at 50 kHz: (a) ADRC, (b) PI control.

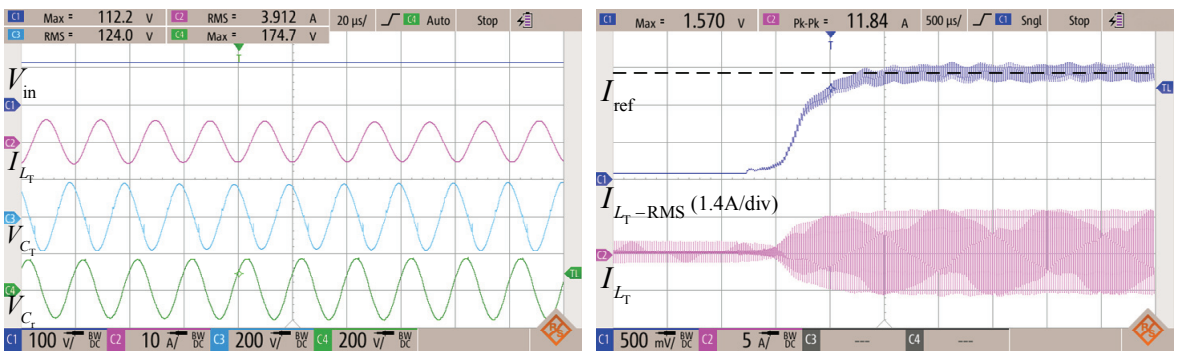

(a)

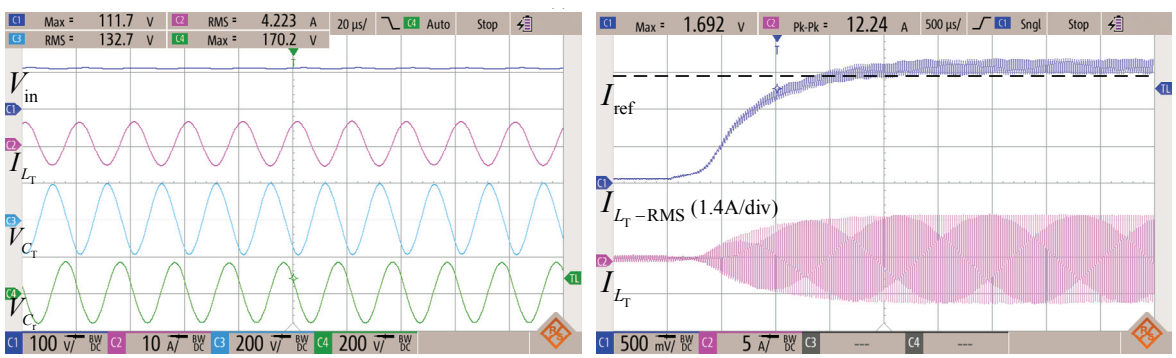

(b)

Fig. 13. Measured DC input voltage, resonant waveforms, and the step response of an IPT system with $f_T = 50$kHz, which is equal to f_0: (a) ADRC, (b) PI control.

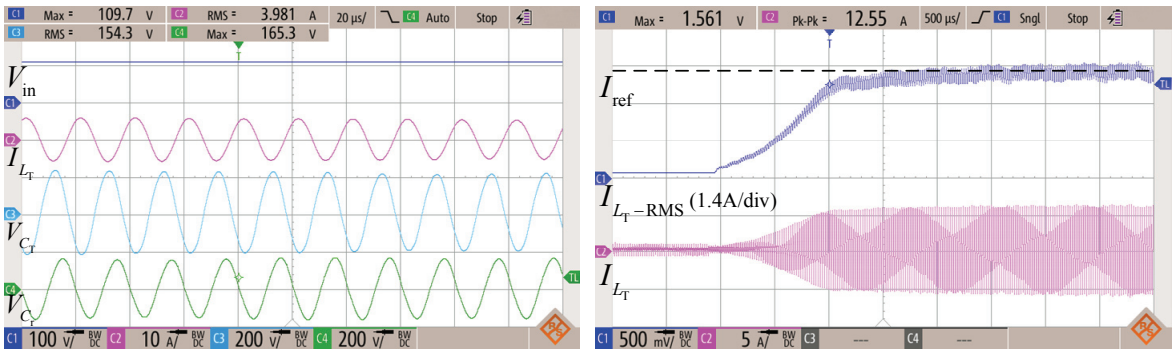

(a)

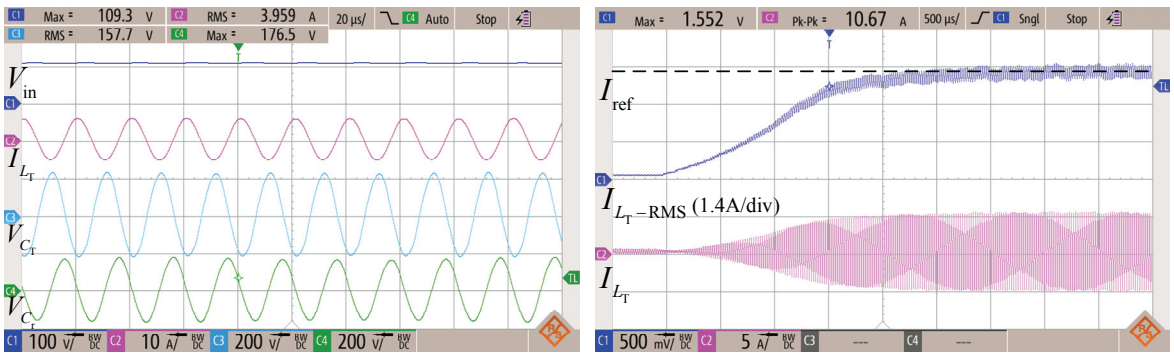

(b)

Fig. 14. Measured DC input voltage, resonant waveforms, and the step response of an IPT system with $f_T = 56\text{kHz}$, while f_0 remains at 50 kHz: (a) ADRC, (b) PI control.

f_0 stays at 50 kHz, while the Tx tanks with three different resonant frequencies are considered. That is, $f_T = 46\text{kHz}$ (8% lower than the working frequency), $f_T = 50\text{kHz}$ (equal to the working frequency) and $f_T = 56\text{kHz}$ (12% higher than the working frequency), as listed in Table I.

In Figs. 12-14 and in all of the following figures, I_{L_T} is the Tx resonant current, I_{L_T-RMS} is the measured RMS current of I_{L_T}, the dash line is the reference input of the Tx resonant current I_{ref}, V_{in} is the measured DC input voltage of the Tx inverter, and V_{C_T} and V_{C_r} are the Tx and Rx resonant capacitor voltages, respectively. From the resonant waveforms in Figs. 12-14, it is possible to directly calculate the transfer power of the Tx coils in three different resonant frequencies under ADRC and PI control, and to obtain the max magnitude of V_{C_r}. Hence, Table II represents the power transmission of the IPT system.

From Table II, it can be seen that the IPT system maintains a transfer power range of 400W-630W under different conditions. Given certain values of I_{ref}, the IPT system still achieves a different Tx transfer power under three different resonant frequencies due to frequency drift. In addition, the transfer power becomes larger when f_T increases. Moreover, when $f_T = 46\text{kHz}$ or $f_T = 50\text{kHz}$, the max magnitude of V_{C_r} under ADRC is also larger than that under the PI control, which demonstrates that the proposed ADRC is effective for IPT systems and may be more efficient than the PI control.

TABLE II
POWER TRANSMISSION OF AN IPT SYSTEM

Tx resonant frequency		46kHz	50kHz	56kHz
Tx transfer power(W)	ADRC	412.4	485.0	614.3
	PI	427.0	560.4	624.3
Max magnitude of V_{C_r}(V)	ADRC	175.6	174.7	165.3
	PI	163.9	170.2	176.5

As for a step response of I_{L_T-RMS}, according to the right side of Figs. 12-14, both of the step responses under ADRC and the PI control have no overshoot to ensure device safety. However, the IPT system with ADRC can achieve a settling time of less than 1ms in Fig. 12, while the settling times of the IPT system with the PI control are all over 1ms, and even reach nearly 2ms in Fig. 14. Hence, it is obvious that the IPT system with ADRC provides a faster dynamic speed while maintaining the same steady-state performance as that with the PI in all cases, especially when $f_T = 50\text{kHz}$ or $f_T = 56\text{kHz}$.

B. Load Disturbance

The responses of I_{L_T-RMS} with ADRC and those with PI control in the presence of load disturbances are presented in this part. Similarly, a load disturbance experiment was conducted under three different Tx resonant frequencies of

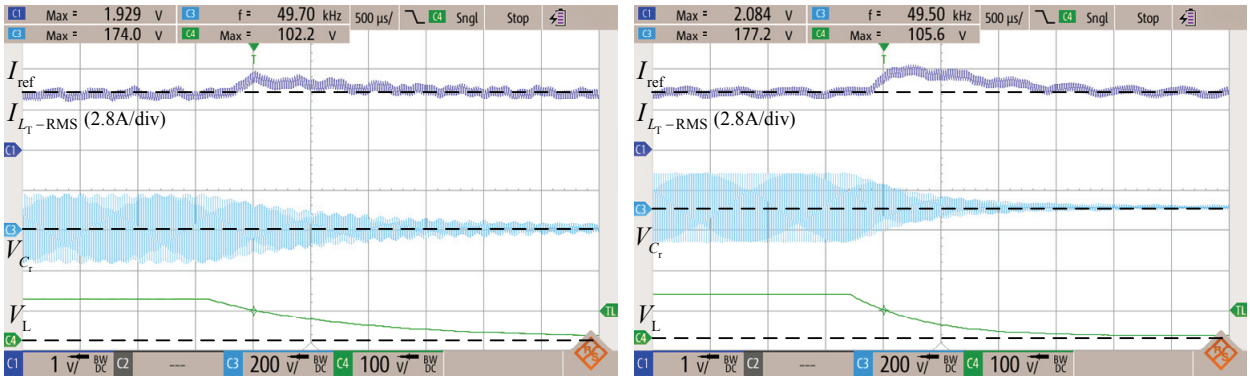

(a) (b)

Fig. 15. Measured RMS of the Tx resonant current, Rx capacitor voltage, and load voltage of an IPT system with $f_T = 46\text{kHz}$ when R_L is changed from 152Ω to 1.974Ω: (a) ADRC, (b) PI control.

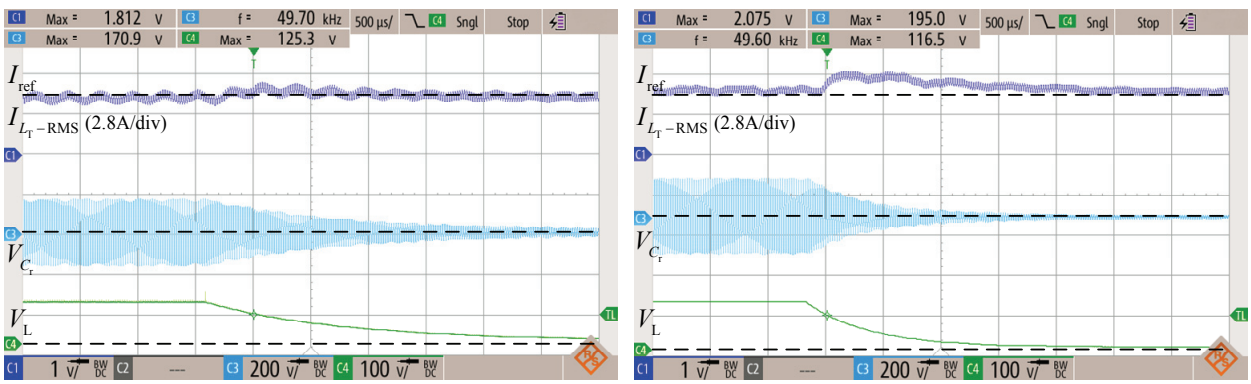

(a) (b)

Fig. 16. Measured RMS of the Tx resonant current, Rx capacitor voltage, and load voltage of an IPT system with $f_T = 50\text{kHz}$ when R_L is changed from 152Ω to 1.974Ω: (a) ADRC, (b) PI control.

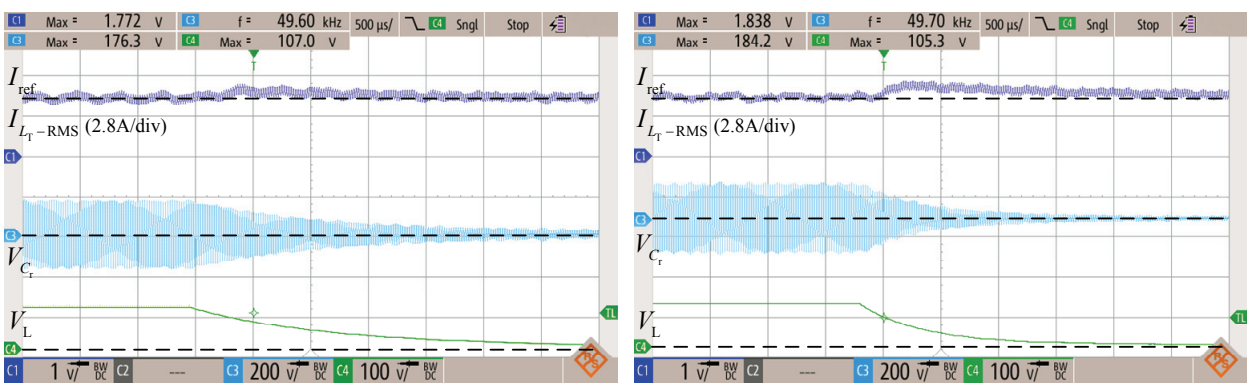

(a) (b)

Fig. 17. Measured RMS of the Tx resonant current, Rx capacitor voltage, and load voltage of an IPT system with $f_T = 56\text{kHz}$ when R_L is changed from 152Ω to 1.974Ω: (a) ADRC, (b) PI control.

46kHz, 50kHz and 56kHz. The corresponding results are presented in Fig. 15, Fig. 16 and Fig. 17, respectively. A load resistor R_L paralleled with a 2Ω resistor, which made the R_L go from 152Ω to 1.974Ω, was employed as the load disturbance in the experiments.

In Figs. 15-17, V_L is the load voltage, which demonstrates the ultimate transfer power to the load. From Figs. 15-17, both the IPT system with ADRC and that with the PI control can provide stable responses against load disturbances. However, the IPT system with ADRC provides lower settling times than that with the PI control in all of the experimental cases. In addition, the fluctuations of I_{L_T-RMS} under ADRC

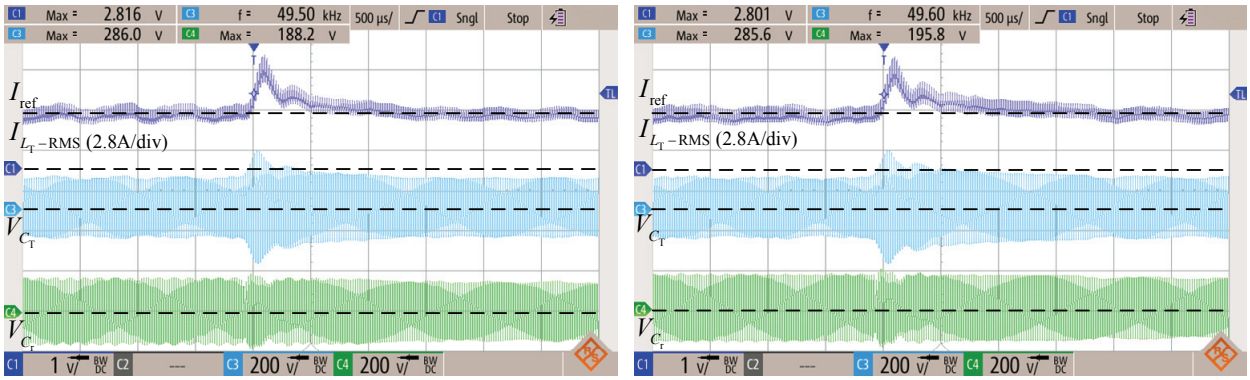

(a) (b)

Fig. 18. Measured RMS of Tx resonant current, and resonant capacitors voltage of IPT system with $f_T = 46$kHz, when C_r is changed from 0.1μF to 0.122μF: (a) ADRC, (b) PI.

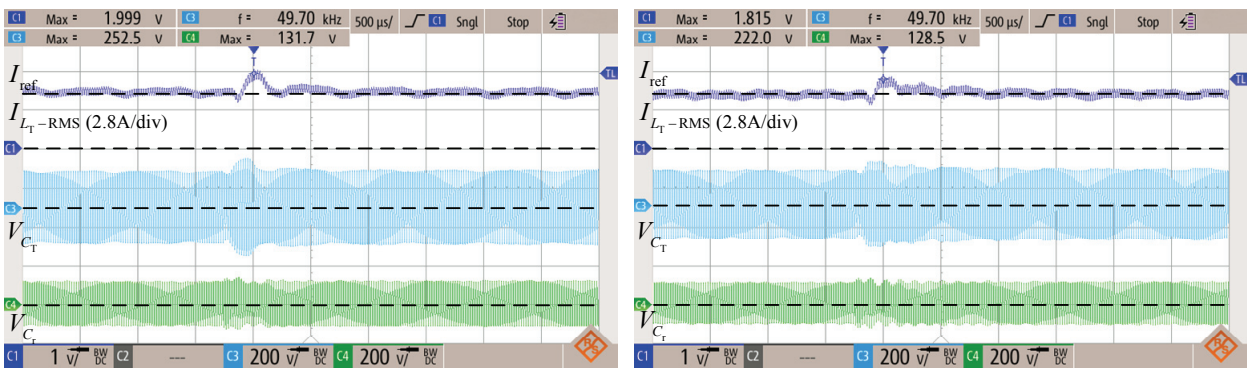

(a) (b)

Fig. 19. Measured RMS of Tx resonant current, and resonant capacitors voltage of IPT system with $f_T = 50$kHz, when C_r is changed from 0.1μF to 0.122μF: (a) ADRC, (b) PI.

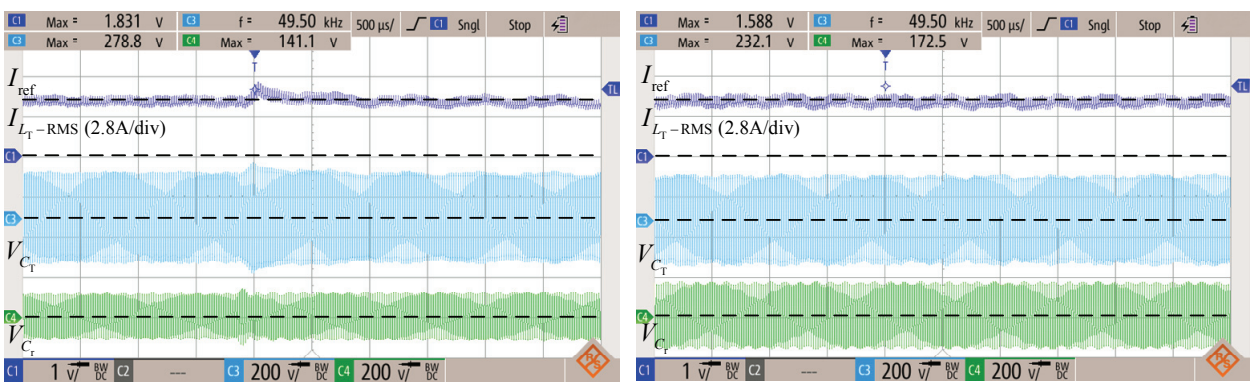

(a) (b)

Fig. 20. Measured RMS of Tx resonant current, and resonant capacitors voltage of IPT system with $f_T = 56$kHz, when C_r is changed from 0.1μF to 0.122μF: (a) ADRC, (b) PI.

are also smaller than those under the PI control. Theoretically, a load disturbance has the largest influence on an IPT system when $f_T = f_0$ as shown in Fig. 16. However, the IPT system with ADRC still retains a strong robustness against disturbances. In this way, the experimental results demonstrate that the proposed ADRC is very useful for IPT systems to maintain robustness against load disturbances.

C. Rx Resonant Capacitor Disturbance

In this section, an IPT system with ADRC and one with the PI control were further tested against Rx resonant capacitor variations under three different Tx resonant frequencies 46kHz, 50kHz, and 56kHz. The Rx resonant capacitor paralleled with a 0.022μF capacitor is employed, and the

corresponding results are shown in Fig. 18, Fig. 19 and Fig. 20, respectively.

Paralleled with a $0.022\,\mu F$ capacitor, the Rx resonant capacitor C_r goes from $0.1\mu F$ to $0.122\mu F$, which makes the resonant frequency of the Rx tank 45.5 kHz. In Fig. 18, when $f_T = 46kHz$, the Rx resonant capacitor disturbance causes a large overshoot in both the IPT system with ADRC and that with the PI control. In addition, the magnitude of the overshoot gradually decreases when f_T changes to 50kHz and then to 56kHz. This phenomenon is due to the fact that, when $f_T = 46kHz$, the Rx resonant frequency change to 45.5 kHz is the closest frequency to the Tx resonant frequency that can cause the largest coupling influence to the Tx side.

From Figs. 18-20, it can be seen that IPT systems with ADRC and PI control can both settle to new steady states within 1ms when $f_T = 46kHz$, and even within $500\mu s$ when $f_T = 50kHz$ or $56kHz$. Moreover, IPT systems with ADRC and PI control both have similar dynamic speeds and steady-state responses to Rx resonant capacitor disturbances. It should be noted that the fluctuations of the IPT system with an ADRC controller in Fig.19 and Fig. 20 are higher than those with a PI controller. According to Fig.8 and Fig.9, this phenomenon is due to the fact that when a frequency drift occurs, the IPT system with ADRC is more sensitive to Rx side disturbances than the original system. Moreover, the parameter tuning of ADRC was determined to obtain a fast dynamic response speed with allowed fluctuations. This suggests that the proposed ADRC method for IPT systems can be applied to IPT systems with middle range power to ensure robustness against parameter disturbances.

It can be concluded from the above experimental results and discussions that IPT systems with ADRC can provide a fast response, and exhibit strong robustness against load disturbances and parameter variations. Furthermore, IPT systems with ADRC can still perform well in cases where the working frequency deviates from the resonating frequency. This suggests that ADRC can be a suitable solution for IPT systems with frequency drifts, which are common in practical working situations.

V. Conclusions

In this paper, an ADRC based control strategy was proposed for IPT systems. To design the required ADRC, a small-signal model of the employed LC series-compensative IPT system was derived by using GSSA, which can simplify the mathematic model of the IPT system. Then a suitable ADRC for the LC series-compensative IPT system was designed to derive a simplified control framework for an IPT system with ADRC. In addition, the robustness of the proposed close-loop system was analyzed. Finally, the proposed ADRC method for an IPT system is demonstrated through experiments and discussions. It has been verified that, despite the nonlinear characteristics of IPT systems, IPT systems with ADRC can provide a fast response, and exhibit strong robustness against load disturbances and parameter variations. Furthermore, it has also been verified that ADRC can be suitable for IPT systems with frequency drifts. Without special requirements being placed on the IPT system structure, ADRC is applicable to many kinds of IPT systems with the general system structure shown in Fig. 1, such as the dynamic EV charging systems.

References

[1] W. Ejaz, M. Naeem, A. Shahid, A. Anpalagan, and M. Jo, "Efficient energy management for the internet of things in smart cities," *IEEE Commun. Mag.*, Vol.55, No.1, pp. 84-91, Jan. 2017.

[2] M. Junil, H. Hyeonseok, J. Byeonghak, C. K. Kwon, T.G. Kim, and S.W. Kim, "Design and implementation of a high-efficiency 6.78 MHz resonant wireless power transfer system with a 5W fully integrated power receiver," *IET Power Electron.*, Vol. 10, No. 5, pp. 577-587, Apr. 2017.

[3] H. Mei, K. Thackston, R. Bercich, J. Jefferys, and P. Irazoqui, "Cavity resonator wireless power transfer system for freely moving animal experiments," *IEEE Trans. Biomed. Eng.*, Vol. 64, No. 4, pp. 775-785, Apr. 2017.

[4] B. Lee, M. Kiani, and M. Ghovanloo, "A triple-loop inductive power transmission system for biomedical applications," *IEEE Trans. Biomed. Circuits Syst.*, Vol. 10, No. 1, pp. 138-148, Feb. 2016.

[5] S. Moon and G. W. Moon, "Wireless power transfer system with an asymmetric four-coil resonator for electric vehicle battery chargers," *IEEE Trans. Power Electronics*, Vol. 31, No. 10, pp. 6844-6854, Oct. 2016.

[6] Q. W. Zhu, L. F. Wang, Y. J. Guo, C. L. Liao, and F. Li, "Applying LCC compensation network to dynamic wireless EV charging system," *IEEE Trans. Ind. Electron.*, Vol. 63, No. 10, pp. 6557-6567, Oct. 2016.

[7] R. K. Mai, Y. Chen, Y. Li, Y. Y. Zhang, G. Z. Gao, and Z. Y. He, "Inductive power transfer for massive electric bicycles charging based on hybrid topology switching with a single inverter," *IEEE Trans. Power Electron.*, Vol. 32, No. 8, pp. 5897-5906, Aug. 2017.

[8] L. L. Tan, S. L. Pan, H. Liu, C. F. Xu, J. P. Guo, and X. L. Huang, "Load detection method for multiple-receiver wireless power transfer systems," *IET Power Electron.*, Vol. 10, No. 14, pp. 1951-1958, Nov. 2017.

[9] Y. Lu, M. Huang, L. Cheng, W. H. Ki, U. Seng-Pan, and R. P. Martins, "A dual-output wireless power transfer system with active rectifier and three-level operation," *IEEE Trans. Power Electron.*, Vol. 32, No. 2, pp. 927-930, Feb. 2017.

[10] M. Barati and M. Yavari, "A power efficient buck-boost converter by reusing the coil inductor for wireless bio-implants," *Int. J. Circuit Theory Appl.*, Vol. 45, No. 11, pp. 1673-1685, Nov. 2017.

[11] W. Zhang, S. C. Wong, C. K. Tse, and Q. H. Chen, "Design for efficiency optimization and voltage controllability of series–series compensated inductive power transfer systems," *IEEE Trans. Power Electron.*, Vol. 29, No. 1, pp. 191-200, Jan. 2014.

[12] T. Diekhans and R. W. De Doncker, "A dual-side controlled inductive power transfer system optimized for large coupling factor variations and partial load," *IEEE Trans. Power Electron.*, Vol. 30, No. 11, pp. 6320-6328, Nov. 2015.

[13] J. D. Wu, C. W. Zhao, Z. Y. Lin, J. Du, Y. H. Hu, and X. N. He, "Wireless power and data transfer via a common inductive link using frequency division multiplexing," *IEEE Trans. Ind. Electron.*, Vol. 62, No. 12, pp. 7810-7820, Dec. 2015.

[14] W. P. Choi, W. C. Ho, and S. Y. R. Hui, "Bidirectional communication techniques for wireless battery charging systems & portable consumer electronics," in *Proc. IEEE APECE*, pp. 2251-2257, 2010.

[15] D. J. Thrimawithana, U. K. Madawala, and M. Neath, "A synchronization technique for bidirectional IPT systems," *IEEE Trans. Ind. Electron.*, Vol. 60, No. 1, pp. 301-309, Jan. 2013.

[16] Y. Sun, P. X. Yan, Z. H. Wang, and Y. Y. Luan, "The parallel transmission of power and data with the shared channel for an inductive power transfer system," *IEEE Trans. Power Electron.*, Vol. 31, No. 8, pp. 5495-5502, Aug. 2016.

[17] Y. Li, C. Zhang, Q. X. Yang, J. X. Li, Y. X. Zhang, X. Zhang, and M. Xue, "Improved ant colony algorithm for adaptive frequency-tracking control in WPT system," *IET Microwaves Antennas & Propagation*, Vol. 12, No. 1, pp. 23-28, Jan. 2018.

[18] F. F. A. Pijl, M. Castilla, and P. Bauer, "Adaptive sliding-mode control for a multiple-user inductive power transfer system without need for communication," *IEEE Trans. Industrial Electron.*, Vol. 60, No. 1, pp. 271-279, Jan. 2013.

[19] P. V. Tuan and I. Koo, "Optimal multiuser MISO beamforming for power-splitting SWIPT cognitive radio networks," *IEEE ACCESS*, Vol. 5, pp. 14141-14153, 2017.

[20] X. F. Yuan, Y. Z. Xiang, Y. Wang, and X. G. Yan, "Neural networks based PID control of bidirectional inductive power transfer system," *Neural Processing Lett.*, Vol. 43, No. 3, pp. 837-847, Jun. 2016.

[21] Z. Zhang, H. L. Pang, C. H. T. Lee, X. K. Xu, X. L. Wei, and J. Wang, "Comparative analysis and optimization of dynamic charging coils for roadway-powered electric vehicles," *IEEE Trans. Magn.*, Vol. 53, No. 11, Nov. 2017.

[22] J. Xiao, C. H. Xu, Q. Zhang, X. B. Huang, J. Y. Qin, "Robust transceiver design for two-user MIMO interference channel with simultaneous wireless information and power transfer," *IEEE Trans. Veh. Technol.*, Vol. 65, No. 5, pp. 3823-3828, May. 2016.

[23] A. Kamineni, G. A. Covic, and J. T. Boys, "A mistuning-tolerant and controllable power supply for roadway wireless power systems," *IEEE Trans. Power Electron.*, Vol. 32, No. 9, pp. 6689-6699, Sep. 2017.

[24] A. Zaheer, M. Neath, H. Z. Beh, and G. A. Govic, "A dynamic EV charging system for slow moving traffic applications," *IEEE Trans. Transport. Electrific.*, Vol. 3, No. 2, pp. 354-369, Jun. 2017.

[25] Q. J. Deng, J. T. Liu, D. Czarkowski, M. Bojarski, E. Asa, and F. De Leon, "Design of a wireless charging system with a phase-controlled inverter under varying parameters," *IET Power Electron.*, Vol. 9, No. 13, pp. 2461-2470, Nov. 2016.

[26] A. K. Swain, M. J. Neath, U. K. Madawala, and D. J. Thrimawithana, "A dynamic multivariable state-space model for bidirectional inductive power transfer systems," *IEEE Trans. Power Electron.*, Vol. 27, No. 11, pp. 4772-4780, Nov. 2012.

[27] A. K. Swain, S. Devarakonda, U. K. Madawala, "Modeling, sensitivity analysis, and controller synthesis of multipickup bidirectional inductive power transfer systems," *IEEE Trans. Ind. Inform.*, Vol. 10, No. 2, pp. 1372-1380, May 2014.

[28] X. Dai and X. Y. Huang, "Study on dynamic accurate modelling and nonlinear phenomena of a push-pull soft switched converter," in *Proc. IEEE CIEA*, pp. 1-4, 2006.

[29] H. Hao, G. A. Covic, and J. T. Boys, "An approximate dynamic model of LCL-based inductive power transfer power supplies," *IEEE Trans. Power Electron.*, Vol. 29, No. 10, pp. 5554-5567, Oct. 2014.

[30] K. Aditya and S. S. Williamson, "Advanced controller design for a series-series compensated inductive power transfer charging infrastructure using asymmetrical clamped mode control," in *Proc. IEEE APECE*, pp. 2718-2724, 2015.

[31] X. Dai, Y. Zou, and Y. Sun, "Uncertainty modeling and robust control for LCL resonant inductive power transfer system," *J. Power Electron.*, Vol. 13, No. 5, pp. 814-828, Sep. 2013.

[32] S. R. Sanders, J. M. Noworolski, X. J. Z. Liu, and G.C. Verghese, "Generalized averaging method for power conversion circuits," *IEEE Trans. Power Electron.*, Vol. 6, No. 2, pp. 251-259, Apr. 1991.

[33] J. P. Xu and C. Q. Lee, "Generalized state-space averaging approach for a class of periodically switched networks," *IEEE Trans. Circuits Syst.—1: Fundam. Theory Appl.*, Vol. 44, No. 11, pp. 1078-1081, Nov. 1997.

[34] J. Q. Han, *Active Disturbance Rejection Control Technique*, National Defense Industry Press, Beijing, 2008.

[35] G. Tian and Z. Q. Gao, "Frequency response analysis of active disturbance rejection based control system," in *Proc. IEEE ICCA*, pp.1595-1599, 2007.

Yanan Wang received her B.S. degree from the Department of Automation, Beijing Institute of Technology, Beijing, China, in 2014, where she is presently working towards her Ph.D. degree. Her current research interests include inductive (contactless) power transfer systems, fractional-order controllers, fractional-order system analysis and renewable energy.

Lei Dong received his B.S. and Ph.D. degrees from the Nanjing University of Aeronautics and Astronautics, Nanjing, China, in 1990 and 2000, respectively. From 2000 to 2002, he was a Postdoctoral Fellow at Tsinghua University, Beijing, China. He is presently working as an Associate Professor at the Beijing Institute of Technology, Beijing, China. His current research interests include power electronics, motion control, microgrids and renewable energy.

Xiaozhong Liao received her B.S. and M.S. degrees in Electrical Engineering from Tianjin University, Tianjin, China, in 1982 and 1984, respectively. She received her Ph.D. degree in Control Sciences and Engineering from the Beijing Institute of Technology, Beijing, China, in 2004. She is presently working as an Associate Dean and as a Full Professor in the Department of Automation, Beijing Institute of Technology. Her current research interests include power electronics, motor drives and renewable energy power conversion.

Xinglong Ju received his B.S. and Ph.D. degrees from the Department of Automation, Beijing Institute of Technology, Beijing, China, in 2010 and 2015, respectively. He is presently working at the Beijing Institute of Space Launch Technology, Beijing, China. His current research interests include inductive (contactless) power transfer systems and renewable energy.

Furong Xiao received his B.S. and Ph.D. degrees from the Department of Automation, Beijing Institute of Technology, Beijing, China, in 2011 and 2017, respectively. He is presently working at Huawei Technologies Co., Ltd., Shenzhen, China. His current research interests include power electronic converters, the control of inverters, renewable energy systems and microgrids.